Effects of aerosol particles on precipitation and cloud parameters over East Africa-Ethiopia using MODIS satellite data: Part 01

Ambachew Abeje Alemu[1,2,*] and Jaya Prakash Raju[1]

[1]Physics Department, Bahir Dar University, PO Box 79, Bahir Dar, Ethiopia
[2]Physics Department, Debre Tabor University, PO Box 272, Debre Tabor, Ethiopia

Received: 15 February, 2024 **Accepted**: 05 March, 2024 **Published**: 21 May, 2024

ABSTRACT

The aerosol-cloud-precipitation interactions – ACPIs - are uncertain that show a large spatiotemporal variability in their magnitude. These things happen because of the effects of aerosol particles on precipitation and cloud parameters, environmental and meteorological conditions, industrial and agricultural influences, and other human influences and natural factors in each ecological functional area. For this study, aerosol and cloud data were retrieved from the Moderate Resolution Imaging Spectroradiometer MODIS sensors. These comprised of the aerosol optical depth AOD, Ångström exponent AET, atmospheric water vapor AWV, mean cloud fraction CFM, cloud top pressure CTP, and cloud top temperature CTT. Precipitation data is comprised of 3B43 products sourced from Tropical Rainfall Measuring Mission TRMM and the outgoing long-wave radiation OLR flux is comprised of Clouds and Earth‘s Radiant Energy System CERES satellite instruments. The study covers sixteen sites in East Africa-Ethiopia with neighboring countries - Eritrea, Djibouti, and South Sudan clustered into four regions for the periods of 2001–2022 to provide detailed information on the aerosol particles spatiotemporal effects on clouds and precipitation. The increase-decrease AWV, CFM and PPT fluctuations are with AOD opposing OLR, CTP and CTT. The parameters are oriented towards western part mostly in the southwest region of the study area. The minima values were found at the southeast cluster in 2022 for all AOD, AWV and CFM; in 2010 for PPT and OLR and in 1999 and for OLR with their maxima at northeast cluster in 2010 for AOD, AWV and CFM; in 2009 for PPT; and in 2011 and 2022 for CTP and CTT from both instruments. Accordingly, the AOD, AWV, CFM, PPT, CTP and CTT minimum values are 0.22, 1.90, 0.21, 1.15, 253.86, 504.53 and 257.73 for Terra and 0.18, 1.91, 0.27, 252.14, 533.43 and 262.94 for Aqua, and the maxima are 0.35, 2.33, 0.33, 2.26, 271.23, 619.08 and 268.49 for Terra and 0.35, 2.35, 0.41, 272.22, 640.07 and 272.58 for Aqua, respectively. The parameters OLR and AWV had the lowest optimum significant PCs at the Humera and Dahlak sites whereas the PCs retained based on AET at the Awassa site and AWV at the Dangote site were the highest. Differences in retained PCs point to different atmospheric dynamics responsible for the behavior of climate during various seasons of the year and the spatial coherence arising from both interannual and intraseasonal variability. And our observation using the HYSPLIT model and fire map confirms that transported aerosol particles in the atmosphere show varied source regions, mostly the Arabian desert and the southwest Indian ocean, at different levels.

Keywords: MODIS; TRMM; CERES; AOD; AET; AWV; CFM; CPT; CTT; PPT; OLR; Ethiopia
DOI: https://dx.doi.org/10.4314/ejst.v17i1.3

---

[*] Corresponding author: ambnehabe21@gmail.com; ambaabe@dtu.edu.et

INTRODUCTION

Our atmosphere is an ever-changing system that keeps the Earth inhabitable by absorbing shortwave radiation and re-emitting long-wave radiation. The atmosphere contains gases, aerosol particles, and collections of liquid and solid hygrometers that make up clouds. Atmospheric aerosols are small mixtures of both solid particles and liquid droplets of particulate matter suspended in the atmosphere (Kafle and Coulter, 2013; Grythe, 2017). Their size ranges from a few tens of nanometers to several tens of micrometers, which is to say they are in between the width of the smallest viruses and the diameter of human hair, barely visible to the human eye, with lifetimes ranging from hours to years. These compositions, sizes, and lifetimes of the aerosol particles affect how far they can travel around the world, their interactions with precipitation, clouds, and radiation budgets, and their total potential effects on climate and human health (Okuda, 2013; ; Mushtaq *et al*., 2022; Duffney *et al.,* 2023).

The aerosol particles that are injected directly into the atmosphere through natural and anthropogenic sources are known as ‘primary aerosols’. These include sea spray, biomass burning, incomplete combustion of fossil fuels, volcanic eruptions, wind-driven or traffic-related suspension of the road, soil, mineral dust, sea salt, sand, and biological materials. Secondary aerosol particles are emitted in another form and then become aerosol particles after going through chemical reactions in the atmosphere, such as sulphate aerosols from volcanoes or industrial emissions. All aerosols can also undergo further chemical changes, referred to as ‘aging effects’. They have numerous potential feedback processes that are still poorly understood, making them an essential component of the atmospheric hydrological cycle and its radiation budget (Gaffney *et al*., 2006; Wild and Liepert, 2010; Behera, 2016; Chi *et al.*, 2019).

There is clear and rapidly growing evidence that atmospheric aerosol particles have profound impacts on the thermodynamics and radiative energy budgets of the Earth. The aerosol particles affect the atmosphere: directly by altering the properties of the radiation energy budget through scattering and absorbing the solar radiation; indirectly by affecting the cloud microphysical properties; and semi-directly through the absorbed radiation energy by aerosol particles, which is able to increase the temperature of the surrounding air, resulting in the evaporation of cloud droplets and ice particles (Kafle and Coulter, 2013; Myhre *et al.,* 2013). Therefore, in addition to their radiative effects, aerosol particles act as condensation nuclei for cloud CCN and ice IN formation and can therefore affect precipitation in several ways (Kaufman *et al*., 2000; Andreae and Rosenfeld, 2008; Li *et al.,* 2021).

The aerosol particles-cloud parameters-precipitation interactions attract more attention, so regional as well as global scientific observations are needed to qualify and confirm the situations. From a previous literature review, we found that there are few studies on atmospheric aerosol particles optical properties in East Africa–Ethiopia using ground or satellite data (Getachew, 2009; Homa *et al.,* 2017; Eshet and Raju, 2022). However, to date, no one has reported the effects of aerosol particles on cloud parameters and precipitation using satellite data from the Moderate Resolution Imaging Spectroradiometer MODIS, Tropical Rainfall Measuring Mission TRMM, and Clouds and Earth‘s Radiant Energy System CERES.

The MODIS is a key instrument that consists of Terra and Aqua satellites onboard that provide long-term and continuous measurement of different aerosol properties from a very long time and plays important role in validating and developing new models to predict climate change (Pagano and Durham, 1993; Koukouli *et al*., 2010; Ismael, 2015; Deep *et al.,* 2021). The Terra satellite orbits around the Earth during the morning at 10:30 local time, descending in the north-to-south direction, while Aqua orbits during the afternoon at 13:30 local time, ascending in the south-to-north direction (Levy *et al.,* 2018; Liu *et al*., 2021; Ustin and Middleton, 2021). Both of these instruments capture the same area on the Earth with 36 spectral bands that can observe its surface every 1–2 days (Justice *et al*., 1998; Bekker *et al*., 2014; Verma *et al*., 2019).

The TRMM is a joint space mission in between the National Aeronautics and Space Administration NASA and Japan’s National Space Development Agency NASDA of Japan which is designed to monitor and study tropical and subtropical precipitation and the associated release of energy. By covering the tropical and subtropical regions of the Earth, the TRMM provided important precipitation information using several space-borne instruments to increase our understanding of the interactions between water vapor, clouds, and precipitation that are central to regulating Earth’s climate (Simpson *et al*., 1988; Theon, 1994; Maggioni *et al*., 2016;).

The CERES is a key component of the Earth Observing System EOS, Suomi National Polar-Orbiting Partnership S-NPP, and National Oceanic and Atmospheric Administration NOAA-20 observatories. It also consists of Terra and Aqua satellites with a three-channel radiometer: a shortwave channel, a long-wave channel, and a total channel that measures both solar-reflected radiation at the top of the atmosphere and Earth-emitted radiation from the Earth’s surface (Smith *et al.,* 2011; Loeb *et al*., 2018; Parkinson, 2022).

Hence, in this study, we used the climatological database of the aerosol particles optical properties, namely the aerosol optical depth AOD and Ångström Exponent AET (Toledano *et al.,* 2007; Kumar *et al.,* 2015; Al-Taie *et al*., 2020), and the cloud parameters such as atmospheric water vapor AWV, mean cloud fraction CFM, cloud top pressure CTP, and cloud top temperature CTT (Sporre, 2016; Barthlott and Hoose, 2018) from MODIS, the precipitation PPT (Li *et al.*, 2017; Barthlott and Hoose, 2018) from TRMM, and the outgoing long-wave radiation OLR flux (Myhre *et al.*, 2013; Li *et al.*, 2017) from CERES satellite instruments, to identify the interactions over East Africa-Ethiopia.

MATERIALS AND METHODS

This section outlines research areas and locations selected for the effects of aerosol particles, along with the data source. In addition, this section includes the methods used in this study to fill in the gaps left by other findings from previous work.

The study areas and sites

This research was carried out in East Africa, specifically in Ethiopia. Despite the fact that they have become independent daughter countries, Djibouti and Eritrea, once parts of Ethiopia, and South Sudan were purposively incorporated into the study areas of the research project (Tongco, 2007; Negash, 2019). Sixteen sites, i.e., ten from Ethiopia, three from South Sudan, two from Eritrea, and one from Djibouti, were selected and then divided into four clustered regions: southwest, southeast, northwest, and northeast. Figure 1 shows four East African countries, namely Ethiopia, Eritrea, Djibouti, and South Sudan{3–18° N, 24–48° E} which have been taken as the study areas (1,897,129 km^2) of this research, along with details of those sites in their clustered regions. Generally, the study areas and selected sites consisted of both the continental and maritime aerosol particle sources.

Remote sensing data

Remote sensing is the process of obtaining information about objects, areas, or phenomena from a distance without being in physical contact to the object. It includes the use of satellite or aircraft-based sensor technologies to detect and classify objects on the Earth’s surface, in the atmosphere and in oceans (Roughgarden *et al.*, 1991; Silleos, 2000). The high spatial and temporal resolution of satellite remote sensing data is more valuable in most atmospheric science studies. Such measurements are made using different platform sensor configurations (Briffa *et al*., 2020; Freemantle *et al.*, 2020; Zhang *et al.*, 2022). For this study, monthly data obtained at the web portals were used: MODIS https://ladsweb.modaps.eosdis.nasa.gov/search/order/ to retrieve aerosol particles and cloud parameters; CERES https://asdc.larc.nasa.gov/data/CERES/ES4/ to calculate outgoing long-wave flux; and TRMM https://daac.gsfc.

nasa.gov/datasets/TRMM_3B43_7/summary?keywords=TRMM_3B43_7 to find the precipitation. Particularly, we collected the data for the Terra satellites MOD08_M3–61 and Terra-Xtrk_Edition4 from January 2001–December 2022 and for TRMM_3B43 from January 1998–December 2019, all for a period of 264 months, and for the Aqua satellite MYD08_3M–61 and Aqua-Xtrk_Edition4 from July 2002–December 2022 for a period of 246 months.

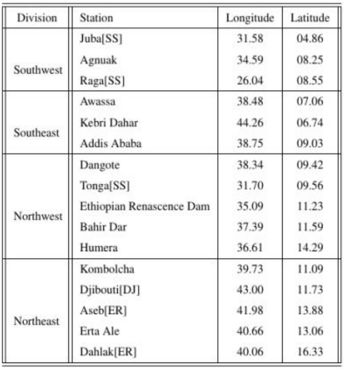

Division	Station	Longitude	Latitude
Southwest	Juba[SS]	31.58	04.86
	Agnuak	34.59	08.25
	Raga[SS]	26.04	08.55
Southeast	Awassa	38.48	07.06
	Kebri Dahar	44.26	06.74
	Addis Ababa	38.75	09.03
Northwest	Dangote	38.34	09.42
	Tonga[SS]	31.70	09.56
	Ethiopian Renascence Dam	35.09	11.23
	Bahir Dar	37.39	11.59
	Humera	36.61	14.29
Northeast	Kombolcha	39.73	11.09
	Djibouti[DJ]	43.00	11.73
	Aseb[ER]	41.98	13.88
	Erta Ale	40.66	13.06
	Dahlak[ER]	40.06	16.33

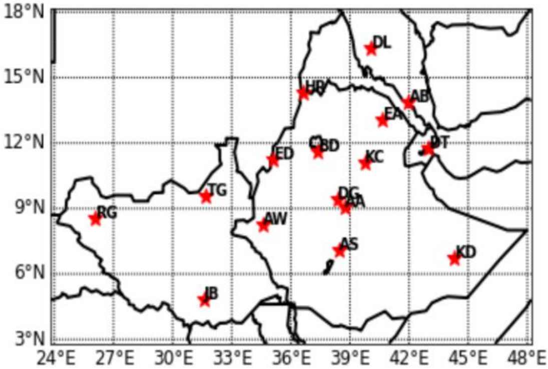

Figure 1. Latitudinal and longitudinal sites of the study area.
Key: JB = Juba; AW = Agnuak; RG = Raga; AS = Awassa; KD = Kebri Dahar; AA = Addis Ababa; DG = Dangote; TG = Tonga; ED = Great Ethiopian Renascence Dam; BD = Bahir Dar; HR = Humera; KC = Kombolcha; DT = Djibouti; AB = Aseb; EA = Erta Ale; DL = Dahlak.

Satellite data retrieval

After browsing the monthly hierarchical data format HDF datasets from the MODIS, TRMM, and CERES websites, we extracted the aerosol, clouds, precipitation, and outgoing long-wave radiation parameters, namely AOD, AWV, CFM, CTP, CTT, PPT, and OLR, and then AET was calculated from AOD both using MATLAB and Python codes. This subsection describes the methods we have been using to derive the details of those parameter retrievals from the satellite datasets.

The parameter aerosol optical depth AOD is the measure of the turbidity-opacity of an environment or a medium (Chen *et al.*, 2020; LeBlanc *et al.*, 2020; Wu *et al.*, 2021). The optical parameter AOD describes section of light removed from a beam by scattering and absorption during its path through the environment (Jin *et al.*, 2023). The AOD values that depend on the sizes, shapes, numbers, concentrations, and the indexes of refraction of the aerosol particles, were related to the wavelength by using the following equation (Eq 1) (Symeonidis, 2017):

$$\mathrm{AOD}(\lambda) = ln\left(\frac{\phi_e^i, \lambda}{\phi_e^t, \lambda}\right) = -ln(\mathrm{T}_\lambda) \tag{1}$$

where: ϕ_e^i, λ is the spectral radiant flux in wavelength received; ϕ_e^t, λ is the spectral radiant flux in wavelength transmitted; T_λ is the spectral transmittance in wavelength λ.

Typically, the AOD (0.55 μm) ranges from 0.05 to 1 over the remote ocean, to 2.0 or even 5.0 during the time of heavy pollution, smoke and dust (Patel and Application, 2016; B. AL-Taie *et al.*, 2020;). For AOD values x_i, the mean $\bar{x}$ could be calculated as follows (Hopkins and Weeks, 1990; Bryhn and Dimberg, 2011):

$$\bar{x} = \sum_{i=1}^{n} \frac{x_i}{n}\ , \tag{2}$$

So, the standard deviation S_d is given by:

$$S_d = \sqrt{\frac{\sum_1^n (x_i - \bar{x})^2}{n}}, \tag{3}$$

And the coefficient of variance CV in % is:

$$\mathrm{CV}(\%) = \frac{S_d}{\bar{x}} x 100\% \tag{4}$$

The parameter Ångström exponent AET is one of the basic parameters that is widely used in atmospheric sciences dealing with the optical properties of aerosol particles. This optical parameter is treated as the indirect measure of the aerosol size in a given column of air. Given the turbidity coefficient β, then AET had been cal culated from the AOD values using equation 5 below (Thapa *et al.*, 2016):

$$\mathrm{AOD}(\lambda) = \beta\lambda^{-\mathrm{AET}} \text{ and then, } \mathrm{AET} = \frac{[ln\{\beta\} - ln\{\mathrm{AOD}(\lambda)\}]}{ln\{\lambda\}} \tag{5}$$

Principal component analysis

The principal component analysis PCA is useful for compressing geophysical data in space-time and separating noise from meaningful data that converts the data to a new coordinate system. PCA involves the transformation of variables into a linear combination of orthogonal components. A series of axes provides location of each data points which represents separate uncorrelated information. The output is covariance matrix denoting transformation coefficients listed in decreasing order of variation. Let P be an m × n matrix of daily data, where m is the number of days and n is the number of stations. This matrix can be decomposed into linear functions of m temporal and n spatial vectors so that the observation P_{ij} on day i at station j is given by the following equation (Stephenson *et al.*, 1999; Gitau *et al.*, 2013; Ledesma and Valero-Mora, 2019):

$$P_{ij} = \sum_{k=1}^{n} a_{ik}\, e_{jk} \Leftrightarrow P = \sum P_{ij} = ae \tag{6}$$

where a_{ik} is the element for day i in k^{th} time vector and e_{jk} the element for station j in k^{th} space vector.

The standardized dataset (A_{ij}) and symmetric n × n correlation matrix C are given as:

$$A_{ij} = \frac{P_{ij} - \bar{P}_j}{S_d} \text{ and } C = \frac{A'A}{m-1} \tag{7}$$

The eigenvectors e are space vectors and the corresponding eigenvalues λ are measures of the explained variance accounted for each eigenvector. Decomposition of correlation matrix into eigenvectors e, and associated eigenvalues λ are obtained by solving:

$$(C - \lambda I)e = 0 \Leftrightarrow |(C - \lambda I)| = 0 \tag{8}$$

Given p × m matrix, $U_m = (u_1, u_2, u_3 \ldots., u_m)$ of PCA loadings. Simplifying with rotation can be achieved by seeking an m × m rotation matrix R to construct rotation of the empirical orthogonal functions REOFs K according to equation 9 (Hansen *et al.,* 2008);

$$K = U_m\beta \tag{9}$$

Maximum factor loadings after rotation that is the correlation coefficients between the variables and factors will be used to determine the relation of selected variables, the parameters for the aerosol optical properties, clouds and precipitations. The simplicity criterion for choosing the rotation matrix for maximization problem is expressed by:

$$\max f(U_m\beta) \tag{10}$$

HYSPLIT trajectory analysis

The HYbrid Single-Particle Lagrangian Integrated Trajectory HYSPLIT model is completed system for computing both simple air parcel trajectories and complex dispersion and deposition simulations. The model calculation method is a hybrid between the Lagrangian approach and the Eulerian approach. The Lagrangian approach uses a moving frame of reference as the air parcel moves from their initial location. And the Eulerian approach uses a fixed three-dimensional grid as a frame of reference (Huang *et al*., 2009; *Lu et al.,* 2022).

An advection and diffusion calculations are made in Lagrangian framework following the transport of the air parcel, while pollutant concentrations are calculated on a fixed grid. Using the model, advection of the particle can be computed from the average of the three-dimensional velocity vectors at the initial position P(t) and first-guess position P'(t+Δt). Respectively, the first guess and final positions are given by Draxler and Hess (1998):

$$P'(t + \Delta t) = P(t) + V(P, t)\Delta t$$
$$P(t + \Delta t) = P(t) + 0.5V(P, t) + V(P', t + \Delta t)\Delta t \qquad (11)$$

RESULTS AND DISCUSSION

After extracting the HDF datasets and collecting their spatial raster AOD, AWV, CFM, CTP, and CTT array values from MODIS, PPT array values from TRMM, and OLR array values from CERES during January 2001–December 2022, the AET values were calculated from the AOD values using the formula described in the methodology section. And then monthly, seasonal and yearly temporal averages were obtained for selected sites clustered into four regions, i.e., southwest, southeast, northwest, and northeast of the study area. In addition, we also discuss the PCA-explained variance and fire-map trajectory model analysis in this section.

Spatial variation

Generally, the East African-Ethiopian climate has been categorized into four major seasons: December–February as winter or *bega* season in Amharic, March–May as spring or *tseday* season in Amharic, June–August as summer or *kiremt* season in Amharic, and September–November as autumn or *belg* season in Amharic (Makokha *et al.,* 2017; Ayanlade *et al.,* 2019; Aga, 2023; Kalisa *et al.,* 2023). In this section, respectively from right to left, bega, tseday, kiremt, belg, and annual, we presented the seasonal as well as the total annual average spatial distribution variations for the study periods 2001–2022. The spatial distribution fluctuations of the parameters we observed in these research findings are shown using Figure 2 for the Terra and Figure 3 for Aqua satellite data.

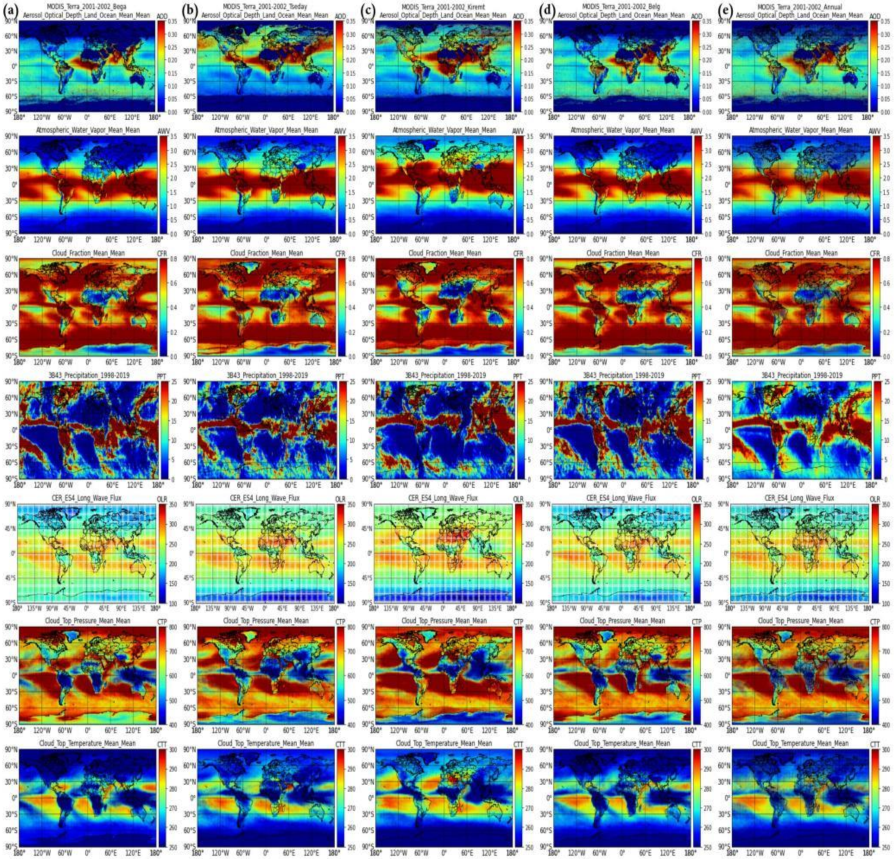

Figure 2. The aerosol optical parameters spatial distribution.

Our observations include the research findings that contain: the aerosol particles optical parameters 0.00≤AOD≤0.35 (1st upper panels); the cloud parameters 0.00≤AWV≤3.50 (2nd panels), 0.00≤CFM≤0.80 (3rd panels), 400.00≤CTP≤800.00 (6th panels), and 2500.00≤CTT≤300.00 (lower panels); the precipitation 0.00≤PPT≤25.00 (only in Terra 4th panels); and the outgoing long-wave radiation flux 100.00≤OLR≤350.00 (the 5th panels) over the globe we take the study area {3–18^0 N, 24–48^0 E} regions with in it.

From both the seasonality and total annual results, we can observe that the parameters are generally oriented towards the western part of the study area regions, mostly in the southwest of the study area regions. The seasonality distribution variation shows that the minimum values are found in the bega season (1st column **a** panels) and the maximum values are in the kiremt season (3rd column **c** panels). The belg season (4th column **d** panels) is the next to have minimum values, while the next maximum values for the kiremt season are in the tesday season (2nd column **b** panels) for both the Terra and Aqua instruments.

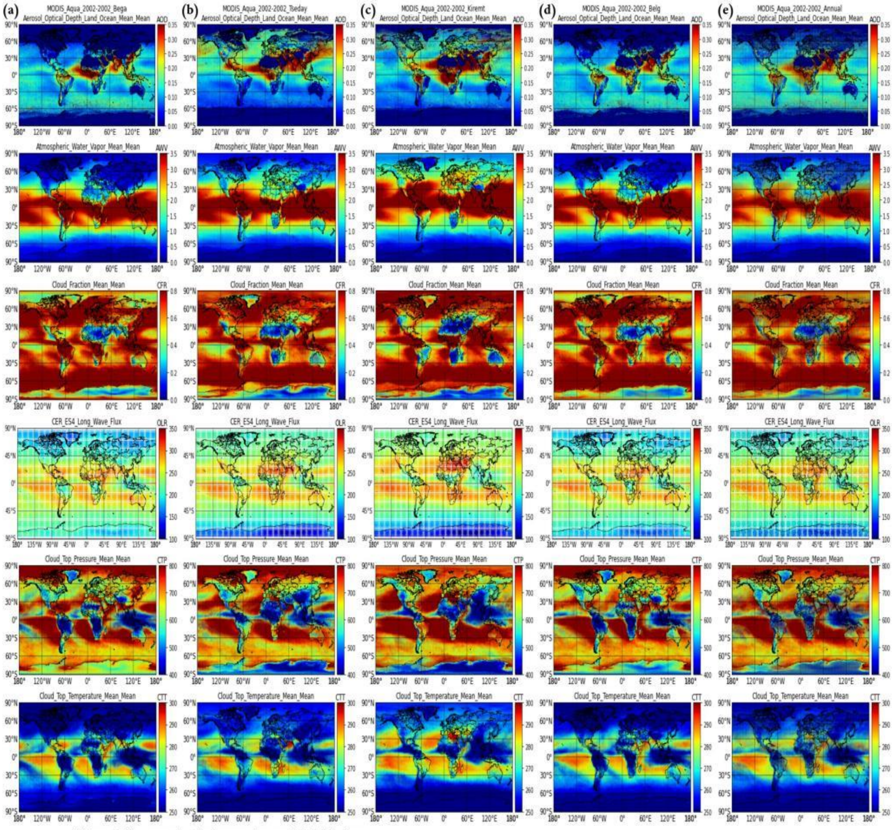

Figure 3. The aerosol optical parameters spatial distribution.

The results are similar to the findings of the studies from the Taklimakan desert in China (Li *et al.*, 2014) and the Nile River Basin in Ethiopia (Getachew *et al.*, 2020) while they contradict the observations of the studies at four selected sites: Addis Ababa, Debre Markos, and Debre Tabor in Ethiopia, and Djibouti in Djibouti (Homa *et al.*, 2017; Eshet and Raju, 2022). In the case of the instruments, greater values are observed from the Aqua instrument and less from the Terra instrument, which contradicts previous observations (Kharol *et al.*, 2011).

So, we can generalize that the findings in our observations show that the parameters have seasonal minimums in the bega season and maximums in the kiremt season, and spatial minimums mostly in 33–42°E and maximums in the southwest of the study area regions, respectively. And the parameters are higher on the Terra instrument relative to the Aqua instrument. Even if there are also contradictory findings to our results, the studies undergone by different scholars we discussed above and others (Li *et al.,* 2014; Ngaina *et al.*, 2014; Boiyo *et al.*, 2018; Torres-Delgado *et al.*, 2021; Kalisa *et al.*, 2023) about the seasonality of the parameters fluctuation, the different local activities, and the long–range aerosol particles transport to the study area regions confirmed our observation.

Monthly variation

This section of the study depicts the results of the total monthly temporal values fluctuations for the aerosol particles, cloud parameters, precipitation, and outgoing long-wave radiation flux we described before. The temporal monthly mean values of the parameters are constructed for each site in the four clustered regions. The results of our observations for the parameters values variations are illustrated in Figure 4 for the Terra and Figure 5 for Aqua satellite data. The increase and decrease fluctuations for the parameters AWV, CFM and PPT are with AOD, while for OLR, CTP and CTT they are vice-versa!

In the southwest cluster (1st column **a** panels), the minimum values for the parameters are observed in South Sudan at the Raga site, while the maximum values are observed in Ethiopia at the Agnuak site for AOD, CFM, CTP, and CTT; in South Sudan at the Juba site for AWV; and at the Raga site for PPT and OLR. For the southeast cluster (2nd column **b** panels), the minimum values are observed in Ethiopia at the Kebri Dahar site AOD, CFM, and PPT. The other minimas in Ethiopia are at the Addis Ababa site for AWV, OLR, CTP, and CTT. And the maximum values are observed in Ethiopia at the Addis Ababa site for AOD and PPT, and still in Ethiopia at the Kebri Dahar site for AWV, OLR, CTP, and CTT. Another maximum value is observed in Eritrea at the Aseb site for CFM. Here, the results we observed and discussed in the southern clustered regions are from both the Terra and Aqua satellite instruments.

In the northwest cluster (3rd column **c** panels), minimum values for the parameters are observed in Ethiopian at the Humera site for AOD, CFM, PPT, OLR, and CTT. The other minima in Ethiopia are at the Dangote sites for AWV and at the Bahir Dar site for CPT.

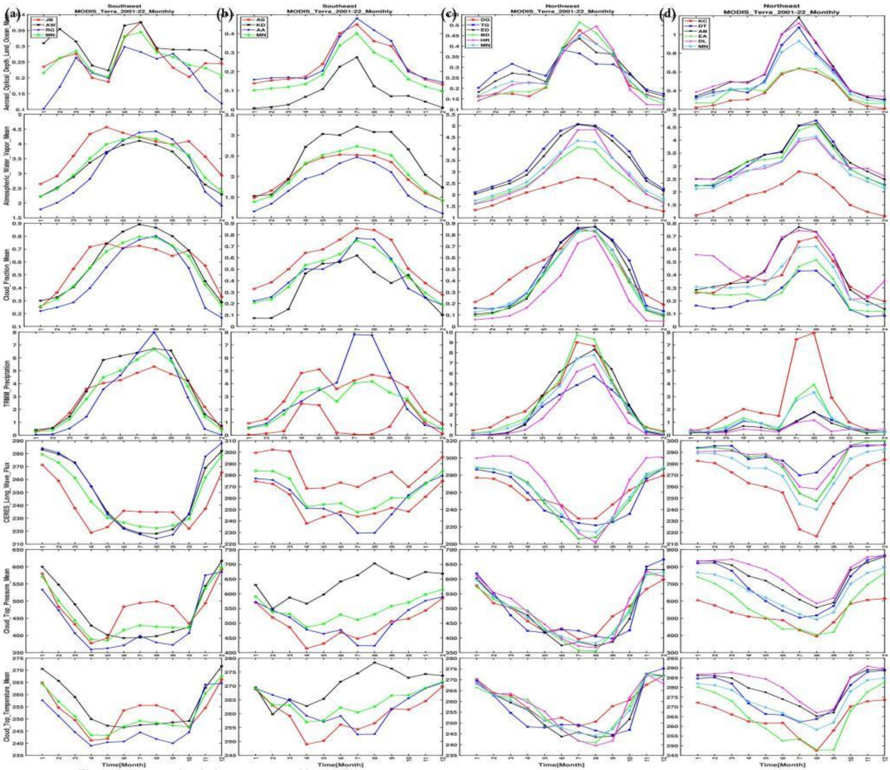

Figure 4. The aerosol optical parameters monthly variation.

When we moved to the northeast cluster (4th column **d** panels), the minimum values for the parameters were observed in Ethiopia at the Kombolcha site for AOD, AWV, OLR, CTP, and CTT. The other minimum values for the parameters were observed in Djibouti at the Djibouti site for CFM and in Eritrea at the Dahlak site for PPT. And the maximum values for the parameters are observed in Eritrea at the Aseb site for AOD and CFM and at the Dahlak site for CPT and CTT. The other maximum values for the parameters are observed in Djibouti at the Djibouti site for AWV and OLR, and also in Ethiopia at the Kombolcha site for PPT. Here, the results we observed and discussed in the northern clustered regions are from both the Terra and Aqua satellite instruments, with some exceptions. Minimum values for the parameters are observed for OLR at the Bahir Dar and the Ethiopian Renaissance Dam sites, and maximum values for CTP and CTT at the Tonga site in the Aqua satellite.

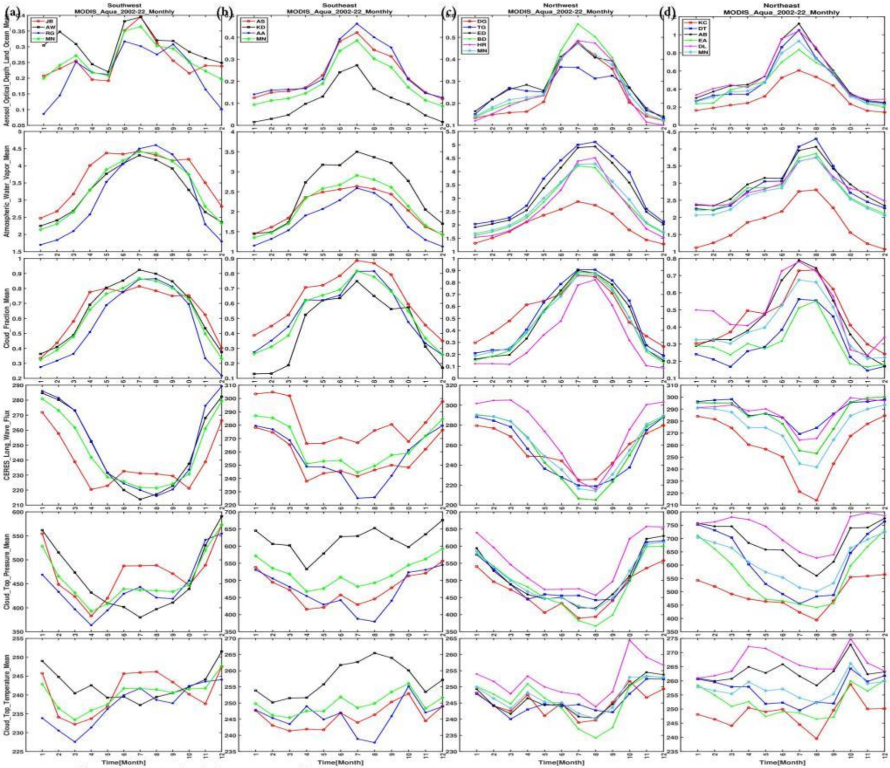

Figure 5. The aerosol optical parameters monthly variation.

In general, for both of the Terra and Aqua instruments: the minimum values are found at the Kebri Dahar site for ADD, at the Kombolcha site for AWV, at the Humera site for both CFM and PPT, all in January and December, while their maximum values were AOD at the Aseb site, AWV at the Tonga site, CFM at the Agnuak site, and PPT at the Bahir Dar site, all in July; the minimum values were found for OLR at the Humera site and CTP at the Bahir Dar site both in August and CTT at the Raga site in March and April, while the maximum OLR value was at the Kebri Dahar site in February; the maximum CTP value was at the Dahlak site in January and December; the maximum CTT value was at the Dahlak site in November. Exceptionally, the minimum values for the OLR were at the Bahir Dar and Ethiopian Renascence Dam sites in July and August for the Terra and Aqua instruments, respectively.

Seasonal variation

The seasonal variations of the parameters at the selected sites clustered into four areas are addressed in this section. The evolution of these parameters estimated from the study periods of 2001–2022 are shown respectively in Figures 6 and 7 for the Terra and Aqua satellite data together with their corresponding total average means. The minimum values for the parameters AOD, AWV, CFM, and PPT were found in the bega season, their maximum values in the kiremt season, while the minimum values for the parameters OLR, CTP and CTT in the kiremt season, and their maximum values were found in the bega season, which were reversed in all of the clusters and both of the instruments.

In the southwest cluster (1st column **a** panels), the minimum values for the parameters are observed in South Sudan at the Raga site, while the maximum values were observed in Ethiopia at the Agnuak site for AOD, CFM, PPT, CTP, and CTT; in South Sudan at the Raga site for the parameters AWV and OLR. For the southeast cluster (2nd column **b** panels), the minimum values were observed in Ethiopia at the Kebri Dahar site AOD, CFM, and PPT. The other minimas in Ethiopia are at the Addis Ababa site for AWV and OLR, and in Eritrea they were at the Aseb site for CTP and CTT. And the maximum values were observed in Ethiopia at the Addis Ababa site for AOD and PPT, and still in Ethiopia at the Kebri Dahar site for AWV, OLR, CTP, and CTT. Another maximum value was observed in Eritrea at the Aseb site for CFM. Here, the results we observed and discussed in the southern clustered regions were from both the Terra and Aqua satellite instruments.

In the northwest cluster (3rd column **c** panels), minimum values for the parameters were observed in Ethiopia at the Humera site for AOD and CFM and at the Ethiopia Renaissance Dam site for CTT. The other minima in Ethiopia were at the Dangote sites for AWV and at the Bahir Dar site for OLR and CPT. The maximum values for the parameters were observed in Ethiopia at the Bahir Dar site for AOD and PPT and at the Humera sites for OLR and CTT. The other maxima values for the parameters were observed in South Sudan at the Tonga site for AWV, CFM, and CPT. When we moved to the northeast cluster (4th column **d** panels), the minimum values for the parameters were observed in Ethiopia at the Kombolcha site for AOD and AWV and at the Erta Ale site for CTP and CTT. The other minimum values for the parameters were observed in Djibouti at the Djibouti site for CFM and in Eritrea at the Aseb site for PPT and OLR. And the maximum values for the parameters were observed in Eritrea at the Aseb site for AOD and CTP and at the Dahlak site for CFM and CTT. The other maximum values for the parameters were observed in Djibouti at the

Djibouti site for AWV. Still, other values were also observed in Ethiopia at the Kombolcha site for PPT and at the Erta Ale site for OLR. Here, the results we observed and discussed in the northern clustered regions were from both the Terra and Aqua satellite instruments, with some exceptions. Minimum values for the parameters were observed for OLR, CTP and CTT at the Kombolcha and the Ethiopian Renaissance Dam sites, and maximum values for CTP and CTT at the Tonga site in the Aqua satellite.

In general, for both of the Terra and Aqua instruments: the minimum values were found at the Kebri Dahar site for ADD, at the Kombolcha site for AWV, at the Humera site for both CFM and PPT, they were all in bega, while the maximum values are for AOD at the Aseb site, AWV at the Tonga site, CFM at the Agnuak site, and PPT at the Bahir Dar site, they were all in kiremt. And also, the minimum values were found for OLR at the Bahir Dar and Ethiopian Renaissance Dam sites, CTP at the Bahir Dar site and CTT at the Humera site, they were all in Kiremt, while the maximum values were for OLR at the Humera site, CTP and CTT at the Dahlak site they were all in bega. Therefore, almost all of the results in the figures indicate extreme values at similar locales, like those of the observations in Figures 6 and 7, with a few noted exceptions.

Those results are similar to the findings and the reasons in the study from eastern China (Liu *et al.,* 2021). The seasonal results for the parameters were similar to those of the observations made in Austria (Yang *et al.,* 2021), Algeria (Khan *et al.,* 2021), eastern China (Liu *et al.,* 2021), and Hong Kong (Yu *et al.,* 2022), despite the fact that there had been no prior studies on the sites in the clustered regions. The discrepancies we discovered were in the minimums with different data periods and site selections. Furthermore, in the study conducted by Yu *et al.* (2022) the minimum values were primarily at bega and the maximum at kiremt.

Yearly variation

In this section, we summarize the total yearly variations of the parameters for all the selected sites belonging to the four clustered regions. Respectively from top to bottom, the first column (**a** panels) in the error bar in Figures 8 and 9 indicate the yearly variations for parameters AOD, AWV, CFM, PPT, OLR, CTP, and CTT from the Terra and Aqua satellites corresponding to the selected sites in the southwest cluster, and the average of all the sites is also superimposed on all plots. Similarly, the other 2nd, 3rd and 4th columns (**b**, **c** and **d** panels) in the figures produced yearly variations of the parameters for the remaining three clustered regions. The majority of the sites, both in the western and eastern cluster zones, clearly demonstrate interannual variability with frequent minimum and maximum values for parameters, as repeated in the aforementioned figures.

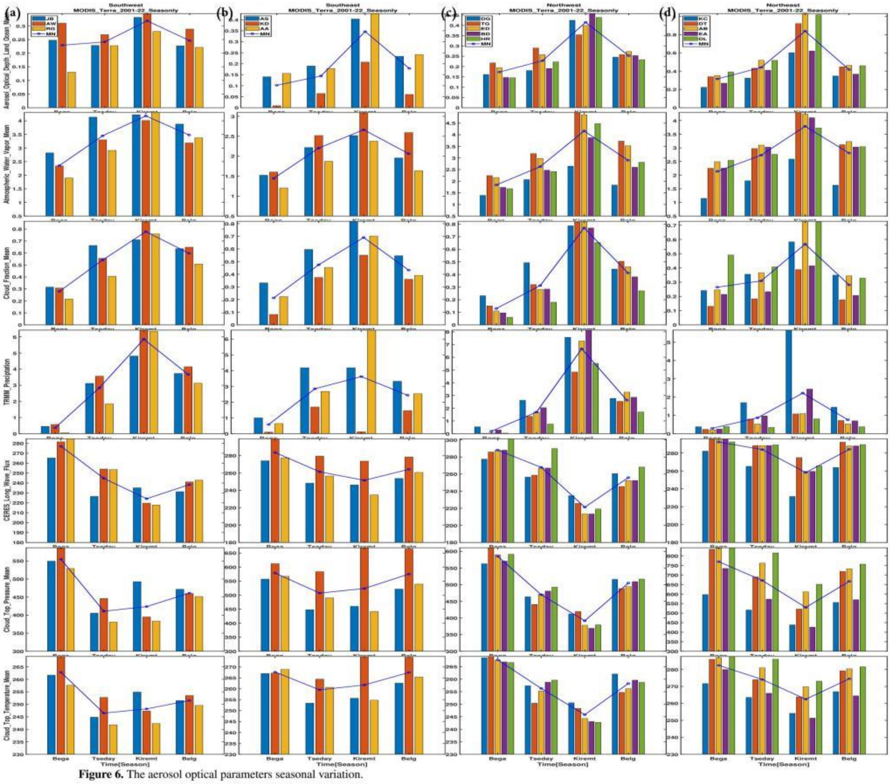

Figure 6. The aerosol optical parameters seasonal variation.

The average of the clustered regions shows the minima at the southeast cluster in 2022 for all AOD, AWV and CFM; in 2010 for PPT and OLR and in 1999 and for OLR with their maxima at the northeast cluster in 2010 for AOD, AWV and CFM; in 2009 for PPT; and in 2011 and 2022 for CTP and CTT from both instruments. Accordingly, the AOD, AWV, CFM, PPT, CTP 295 and CTT minimum values were 0.22, 1.90, 0.21, 1.15, 253.86, 504.53 and 257.73 for Terra and 0.18, 1.91, 0.27, 252.14, 533.43 and 262.94 for Aqua, and the maxima are 0.35, 2.33, 0.33, 2.26, 271.23, 619.08 and 268.49 for Terra and 0.35, 2.35, 0.41, 272.22, 640.07 and 272.58 for Aqua, respectively. Here, the parameter PPT is illustrated only in Figures 8 and the values for all of the parameters we observed in the Aqua satellite were mostly greater than those of the Terra satellite. The values for the parameters were higher in the southern clusters, specifically in the southwest clusters, than in the northern clusters.

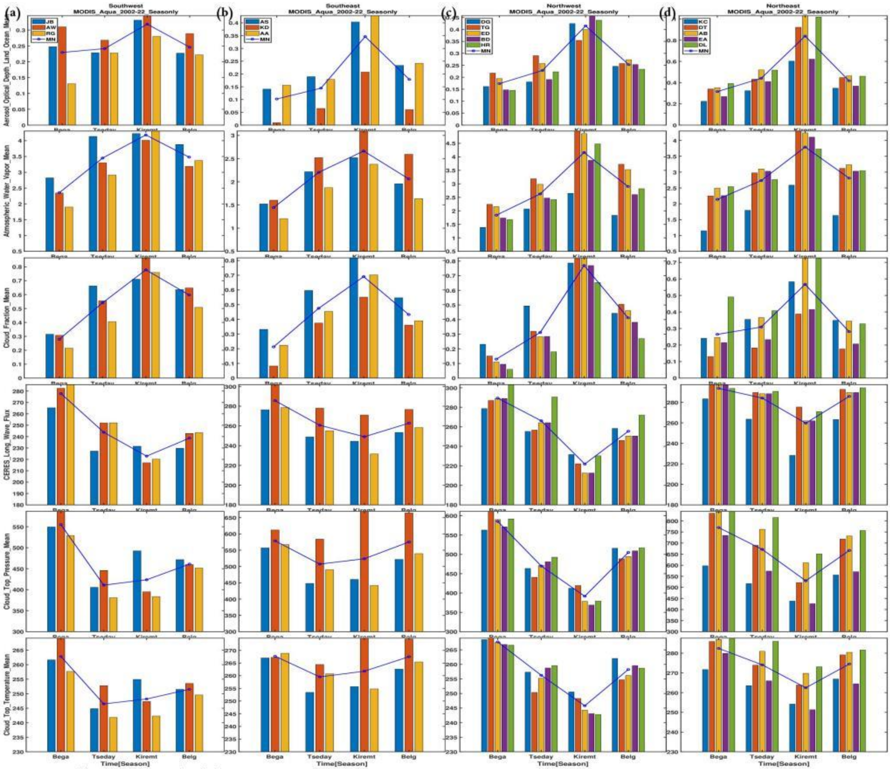

Figure 7. The aerosol optical parameters seasonal variation.

The explained variance

In this study, the PCA analysis was used to evaluate the contribution of selected satellite-derived aerosol particles, clouds, outgoing long-wave radiation flux, and precipitation dataset parameters at 16 selected sites clustered into four regions over East Africa-Ethiopia. Table 1 presents results for the optimum number of the principal component retained based on aerosols, clouds, outgoing long-wave radiation flux, and precipitation datasets. The results in Figures 10 present a detailed analysis to investigate the variability explained by the number of significant PCs retained for aerosol particles, clouds, outgoing long-wave radiation flux, and precipitation parameters.

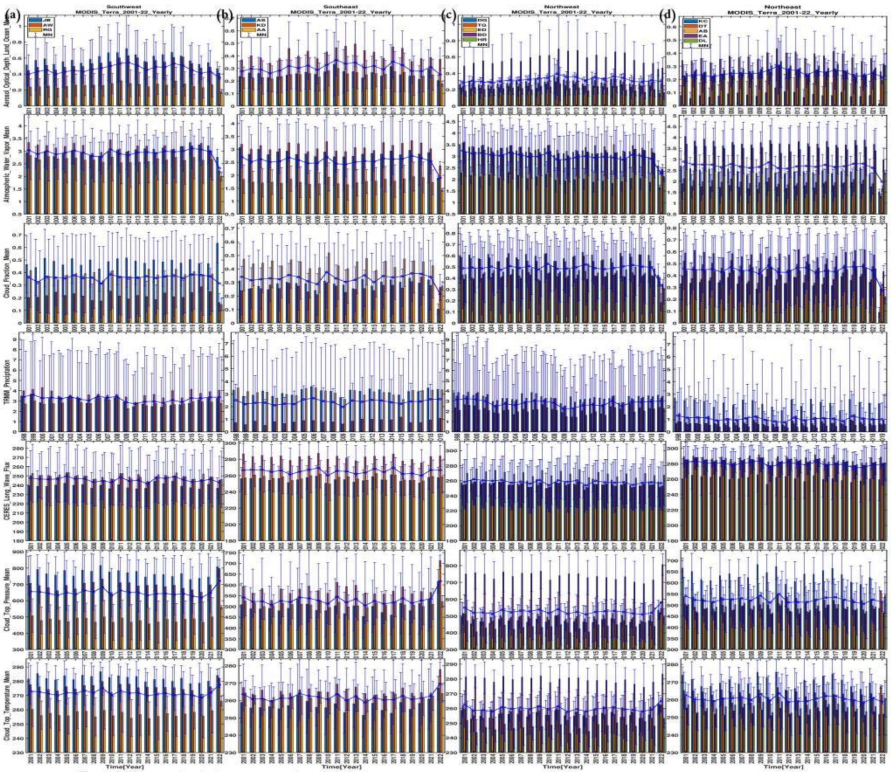

Figure 8. The aerosol optical parameters yearly variation.

The identified PCs were found to be significant at 95% confidence level based on Monte Carlo testing (Ngaina, 2015). Notably, the OLR and AWV parameters, both at the Humera and Dahlak sites, had the lowest optimum significant PCs, which was attributed to the course resolution of the datasets from both of the instruments. The number of significant PCs retained based on AET at the Awassa site and AWV at the Dangote site was highest compared to the other parameters. The differences in retained PCs point to the different atmospheric dynamics responsible for the behavior of climate during the various seasons of the year and the spatial coherence arising from both interannual and intraseasonal variability. Further, the use of seasonal and annual totals provides information on interannual variability only. However, the other studies showed that results from the monthly analysis were better during prolonged rainfall due to high variability (Ininda, 1994; Gitau *et al.*, 2013). According to the findings, the entire East Africa region was classified into eight and nine near homogeneous zones based on the annual and seasonal observed rainfall, respectively (Indeje *et al.*, 2000).

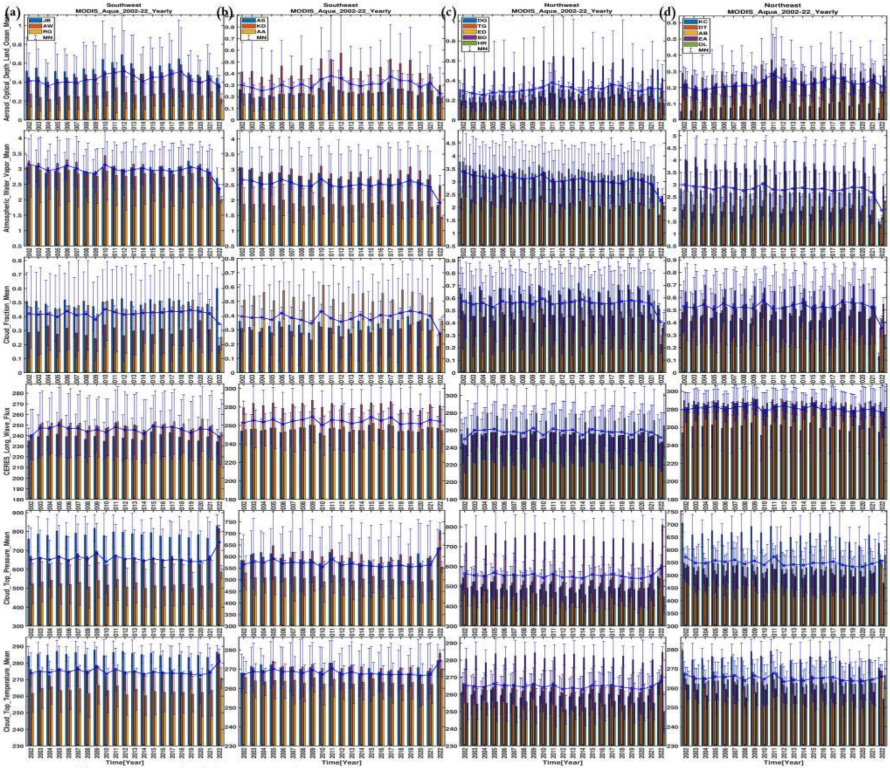

Figure 9. The aerosol optical parameters yearly variation.

The fire-map trajectory

In this research, the backward fire-map trajectory analysis was done using the HYSPLIT model at the Agnuak site from the southwest cluster, at the Kebri Dahar and Addis Ababa sites from the southeast cluster, at the Humera site from the northwest cluster, and at the Aseb site from the northeast cluster. We utilized a five-day backward trajectory analysis to identify the sources of atmospheric aerosol particles at 500–5000 metres above ground-level MAGL. For the selected five location sites: the 2nd row panels for the Agnuak site in 2002, the 3rd row panels for the Kebri Dahar site in 2011, the 4th row panels for the Addis Ababa site in 2015, the 5th row panels for the Humera site in 2011, and the 6th row panels for the Aseb site in

2012, with a high factor loading based on TRMM 3B43 satellite-derived rainfall estimates were utilized.

The 1st row panels in the Figures are to illustrate the fire map trajectories for the sources from the biomass burnings BBs. The HYSPLIT trajectories were computed for the start, June 01 and 16 (the 1st and 2nd columns **a, b** panels); mid, July 01 and 16 (the 3rd and 4th columns **c, d** panels); and end, August 01, 16 and 31 (the 5th, 6th and 7th columns **e, f, g** panels), of the kiremt season, as shown in Figure 10.

At the beginning of the season, the backward trajectories identified the continental source regions as the Arabian Desert and the Indian subcontinent. The selected continental stations included Agnuak, Kebri Dehar, Addis Ababa, and Humera. The locations of the maritime source regions were in the sub-western Indian Ocean, with the selected sink station at the Aseb site. In the middle of the season, the source regions for the study area sites were in the southwest Indian Ocean, Kenya, Madagascar, Uganda, Sudan, and Egypt. At the end of the season, all the source regions for all stations at all levels were located in the Arabian Desert, the southwest Indian Ocean, Central Africa, Kenya, Madagascar, Uganda, Sudan, and Egypt.

Here, the study area regions by themselves were also the source regions at the beginning, middle, and end of the season at all levels. And we observed that there were active fires in all the source regions during the beginning, middle, and end of the season on the fire map projected as in the 1st row panels of the Figures (Figure 11).

Generally, at different levels, transported aerosol particles in the atmosphere show varied source regions. The aerosol particles undergo vertical mixing inland in East Africa-Ethiopia. Further, several high mountains >2000 m are situated near the Great Rift Valley area in East Africa-Ethiopia. They include Mount Kilimanjaro, Mount Kenya, and Mount Rwenzori. These mountains block the eastward transport of the Sahel smoke as well as dust from the Bodele Depression (Washington and Todd, 2005; Fiedler and Tegen, 2014). Therefore, these mixed aerosols accounted for increased rainfall over locations with high factor loadings based on TRMM 3B43 rainfall (Yang and Zeng, 2013).

Here, the study area regions by themselves were also the source regions at the beginning, middle, and end of the season at all levels. And we observed that there were active fires in all the source regions during the beginning, middle, and end of the season on the fire map projected as in the 1st row panels of the Figures (Figure 11).

Table 1: Percentage of explained variance based on AOD in precipitation and cloud parameters.

Clusters		Southwest			Southeast			Northwest					Northeast				
Sites		JB	AW	RG	AS	KD	AA	DG	TG	ED	BD	HR	KC	DT	AB	AE	DL
TERRA	AOD	76.73933	20.23363	3.02705	94.17940	4.27753	1.54307	82.73777	12.01738	3.65045	1.07927	0.51513	90.25404	5.36274	1.96848	1.58128	0.83347
	AET	64.70823	31.88831	3.40346	97.30233	2.42940	0.26827	80.86167	13.72519	3.81542	1.10606	0.49165	87.50381	7.19404	3.09355	1.55495	0.65365
	AWV	89.26286	7.55244	3.18471	84.03200	11.84184	4.12616	95.52147	2.51904	1.27996	0.51779	0.16175	81.70954	14.57567	1.68779	1.46560	0.56140
	CRF	86.71811	9.05469	4.22720	94.73250	4.42521	0.84229	92.96030	3.58475	2.39505	0.61189	0.44802	55.56792	28.39492	7.78548	7.11895	1.13273
	PPT	62.10693	23.50944	14.38362	64.88465	25.39582	9.71953	67.39023	16.98714	9.15673	4.15465	2.31126	77.47822	11.64260	5.92301	3.51182	1.44435
	OLR	88.72757	9.83584	1.43659	85.63301	12.22916	2.13783	94.79371	2.81389	1.77993	0.61246	0.00000	94.90689	2.34225	2.11515	0.63571	0.00000
	CPT	70.23797	16.88900	12.87303	86.87264	11.84006	1.28731	78.36714	13.47516	3.35201	2.68929	2.11639	80.50630	11.44524	4.67903	1.95688	1.41255
	CTT	67.55355	17.80640	14.64005	86.29808	12.29272	1.40920	73.79662	15.64307	4.61335	3.53874	2.40822	71.61495	18.02711	5.84235	2.59034	1.92526
AQUA	AOD	84.70071	12.61905	2.68024	95.42342	3.54012	1.03645	88.94035	7.16094	2.69740	0.87293	0.32838	88.94690	6.16285	2.86151	1.26048	0.76825
	AET	76.99748	19.53934	3.46318	95.73084	3.89758	0.37157	86.89722	8.89579	3.13974	0.73780	0.32946	88.46001	6.26736	3.53449	0.92067	0.81748
	AWV	92.53369	4.17327	3.29303	88.65611	9.43300	1.91089	96.57223	1.52195	1.26090	0.46834	0.17658	87.97118	7.29076	2.57206	1.33557	0.83042
	CRF	89.88591	7.41667	2.69742	94.08575	4.79364	1.12061	90.48992	5.15982	2.78661	1.40036	0.16330	68.81907	15.17137	8.18359	6.20453	1.62144
	OLR	91.09479	7.34459	1.56061	87.59003	10.87574	1.53423	95.82135	2.14056	1.60456	0.43352	0.00000	94.27929	3.06419	1.99185	0.66467	0.00000
	CPT	45.95326	36.69971	17.34703	69.41749	27.82834	2.75418	81.21971	9.98676	4.37016	2.71255	1.71082	85.13126	7.14464	3.90295	2.27019	1.55096
	CTT	47.81010	37.12246	15.06745	59.73888	36.95421	3.30691	80.83209	9.53087	5.93915	2.18724	1.51065	76.63567	9.26518	8.37120	4.53936	1.18859

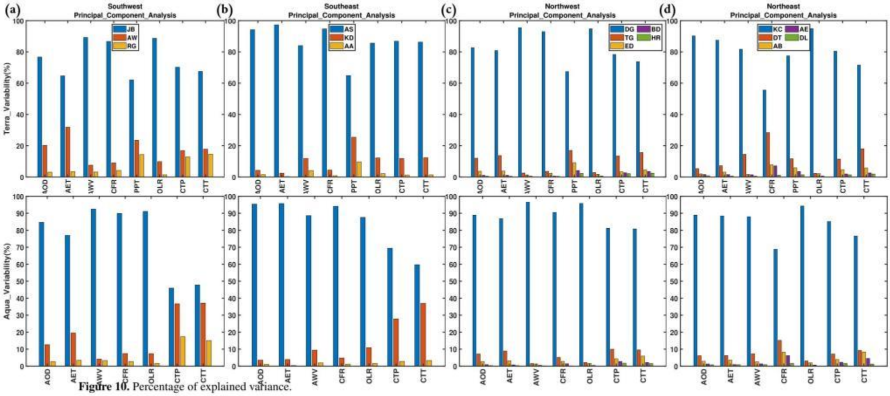

Figure 10. Percentage of explained variance.

Generally, at different levels, transported aerosol particles in the atmosphere show varied source regions. The aerosol particles undergo vertical mixing inland in East Africa-Ethiopia. Further, several high mountains >2000 m are situated near the Great Rift Valley area in East Africa-Ethiopia. They include Mount Kilimanjaro, Mount Kenya, and Mount Rwenzori. These mountains block the eastward transport of the Sahel smoke as well as dust from the Bodele Depression (Washington and Todd, 2005; Fiedler and Tegen, 2014). Therefore, these mixed aerosols accounted for increased rainfall over locations with high factor loadings based on TRMM 3B43 rainfall (Yang and Zeng, 2013).

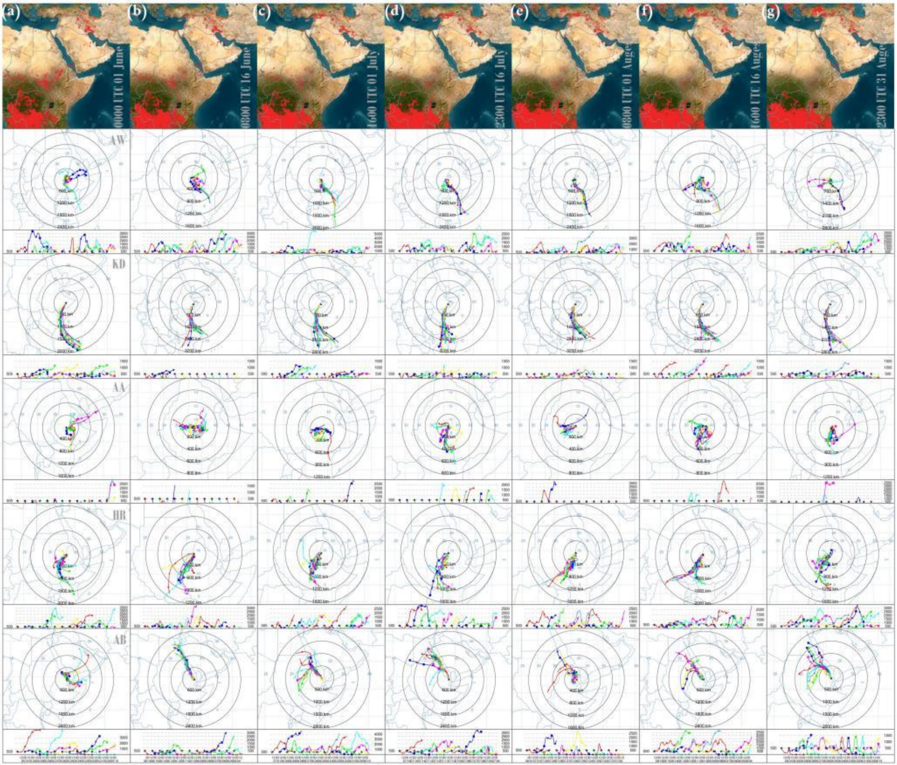

Figure 11. Fire maps and HYSPLIT backward trajectories during start, mid and end of kiremt.

CONCLUSION

The purpose of this study is to investigate the effects of aerosol particles on precipitation and cloud parameters based on the spatiotemporal distribution variations retrieved from the MODIS, TRMM 3B43, and CERES sensors over a period of 22 years (for Terra: January 2001 to December 2022, and for Aqua: July 2002 to December 2022). Those parameter retrievals included the spatial, monthly, seasonal, and yearly values at sixteen selected sites clustered in four regions with their corresponding averages. The main conclusions drawn from our work are as follows:

The seasonality total spatial averaged values for the aerosol particles optical depth parameters were $0.00 \leq AOD \leq 0.35$; for the cloud parameters, they were $0.00 \leq AWV \leq 3.50$, $0.00 \leq CFM \leq 0.80$, $400.00 \leq CTP \leq 800.00$, and $2500.00 \leq CTT \leq$

300.00; for precipitation, they were $0.00 \leq PPT \leq 25.00$; and for the outgoing long-wave radiation flux, they were $100.00 \leq OLR \leq 350.00$, with their minimums occurring in the bega season and their maximums occurring in the kiremt season. Across the globe, we consider the study area {3–18^0 N, 24–48^0 E} regions within it.
The minimum monthly values were found at the Kebri Dahar site for ADD, at the Kombolcha site for AWV, at the Humera site for both CFM and PPT, they all in January and December, while their maximum values were AOD at the Aseb site, AWV at the Tonga site, CFM at the Agnuak site, and PPT at the Bahir Dar site, they all in July; the minimum values were found for OLR at the Humera site and CTP at the Bahir Dar site both in August and CTT at the Raga site in March and April, while the maximum OLR value was at the Kebri Dahar site in February; the maximum CTP value was at the Dahlak site in January and December; the maximum CTT value was at the Dahlak site in November. Exceptionally, the minimum values for the OLR were at the Bahir Dar and Ethiopian Renaissance Dam sites in July and August for the Terra and Aqua instruments, respectively.

The minimum values were found at the Kebri Dahar site for ADD, at the Kombolcha site for AWV, and at the Humera site for both CFM and PPT; they were all in bega, while the maximum values were for AOD at the Aseb site, AWV at the Tonga site, CFM at the Agnuak site, and PPT at the Bahir Dar site; they were all in kiremt. And also, the minimum values were found for OLR at the Bahir Dar and Ethiopian Renaissance Dam sites, CTP at the Bahir Dar site, and CTT at the Humera site; they were all in kiremt, while the maximum values were for OLR at the Humera site, CTP, and CTT at the Dahlak site; they were all in bega.

The total annual average variation shows the minima at the southeast cluster in 2022 for all AOD, AWV and CFM; in 2010 for PPT and OLR and in 1999 and for OLR with their maxima at the northeast cluster in 2010 for AOD, AWV and CFM; in 2009 for PPT; and in 2011 and 2022 for CTP and CTT from both instruments. Accordingly, the AOD, AWV, CFM, PPT, CTP and CTT minimum values were 0.22, 1.90, 0.21, 1.15, 253.86, 504.53 and 257.73 for Terra and 0.18, 1.91, 0.27, 252.14, 533.43 and 262.94 for Aqua, and the maxima were 0.35, 2.33, 0.33, 2.26, 271.23, 619.08 and 268.49 for Terra and 0.35, 2.35, 0.41, 272.22, 640.07 and 272.58 for Aqua, respectively.

The OLR and AWV parameters, both at the Humera and Dahlak sites, had the lowest optimum significant PCs, whereas the PCs retained based on AET at the Awassa site and AWV at the Dangote site were the highest compared to the other parameters. The differences in retained PCs point to the different atmospheric dynamics responsible for the behavior of climate during the various seasons of the year and the spatial coherence arising from both interannual and intraseasonal variability. And our observation using the HYSPLIT model and fire map confirms that transported aerosol particles in the atmosphere show varied source regions, mostly the Arabian desert and the southwest Indian ocean, at different levels.

ACKNOWLEDGMENTS

This research was supported by two Ethiopian higher education institutions, namely Bahir Dar University and Debre Tabor University, which gave the study a chance and sponsored it. The authors would like to thank the NASDA-NASA HDF-EOS Tools and Information Center Help Team for providing the MODIS, TRMM and CERES data on aerosol-cloud-precipitation parameters interactions.

REFERENCES

Aga, M.T. (2023). Climate and seasons in Ethiopia, Ethiopia's first and largest blog network. https://allaboutethio.com/tclimate.html. Online; accessed 19-July-2023.

Al-Taie, K.B., Rajab, J.M and Al-Salihi, A.M. (2020). Climatology and classification of aerosols based on optical properties over selected stations in Iraq. *AIP Conference Proceedings* **2290**: 050041. AIP Publishing LLC, 2020.

Andreae, M and Rosenfeld, D. (2008). Aerosol–cloud–precipitation interactions. Part 1. The nature and sources of cloud-active aerosols. *Earth Science Reviews* **89**: 13–41.

Ayanlade, A., Atai, G and Jegede, M.O. (2019). Spatial and seasonal variations in atmospheric aerosols over Nigeria: assessment of influence of intertropical discontinuity movement. *Journal of Ocean and Climate* **9**: 175931311882030

Barthlott, C and Hoose, C. (2108). Aerosol effects on clouds and precipitation over central Europe in different weather regimes. *Journal of the Atmospheric Sciences* **75:** 4247–4264.

Behera, S. (2016). Estimation of aerosol optical depth using MODIS satellite data and its relation with particulate matter concentration in the mining regions, Ph.D. thesis, National Institute of Technology Rourkela.

Bekker, A., Farquhar, J and Zerkle, A. (2014). 6.4-Geologic and geochemical constraints on Earth's early atmosphere. In: Treatise on Geochemistry, 2nd Ed. pp. 91–138.

Boiyo, R., Kumar, K.R and Zhao, T. (2018). Optical, microphysical and radiative properties of aerosols over a tropical rural site in Kenya, East Africa: source identification, modification and aerosol type discrimination. *Atmospheric Environment* **177:** 234–252.

Briffa, J., Sinagra, E and Blundell, R. (2020). Heavy metal pollution in the environment and their toxicological effects on humans. *Heliyon* **6**: e04 691.

Bryhn, A.C and Dimberg, P.H. (2011). An operational definition of a statistically meaningful trend. *PLoS One* **6**: e19 241.

Chen, X., Ding, J., Wang, J., Ge, X., Raxidin, M., Liang, J., Chen, X., Zhang, Z., Cao, X and Ding, Y. (2020). Retrieval of fine-resolution aerosol optical depth (AOD) in semiarid urban areas using Landsat data: A case study in Urumqi, NW China. *Remote Sensing* **12**: 467.

Chi, Y., Zuo, S., Ren, Y and Chen, K. (2019). The spatiotemporal pattern of the aerosol optical depth (AOD) on the canopies of various forest types in the exurban national park: a case in Ningbo city, eastern China. *Advances in Meteorology* **2019:** Article ID 4942827. https://doi.org/10.1155/2019/4942827

Deep, A., Pandey, C.P., Nandan, H., Singh, N., Yadav, G., Joshi, P., Purohit, K and Bhatt, S. (2021). Aerosols optical depth and Ångström exponent over different regions in Garhwal Himalaya, India. *Environmental Monitoring and Assessment* **193**: 1–19.

Draxler, R.R and Hess, G. (1998). An overview of the HYSPLIT_4 modelling system for trajectories. *Australian Meteorological Magazine* **47**: 295–308.

Duffney, P., Stanek, L and Brown, J. (2023). Air pollution: Sources, regulation, and health effects. https://nap.nationalacademies.org/read/12001/chapter/5. Online; accessed 19 July 2023.

Eshet, A and Raju, J.P. (2022). Daily and seasonal variation of aerosol optical depth and angstrom exponent over Ethiopia using MODIS data. *Pollution* **8**: 315–329.

Fiedler, S., Schepanski, K., Knippertz, P., Heinold, B and Tegen, I. (2014). How important are atmospheric depressions and mobile cyclones for emitting mineral dust aerosol in North Africa? *Atmospheric Chemistry and Physics* **17**: 8983–9000.

Freemantle, V., Freemantle, J., Atkinson, D and Treitz, P. (2020). A high spatial resolution satellite remote sensing time series analysis of Cape Bounty, Melville Island, Nunavut (2004–2018). *Canadian Journal of Remote Sensing* **46**: 733–752.

Gaffney, J.S and Marley, N.A. (2006). Urban aerosols and their impacts: lessons learned from the World Trade Center Tragedy. ACS Symposium Series 919, Washington DC. https://pubs.acs.org/doi/pdf/10.1021/bk-2006-0919.fw001. Online; accessed 19 July 2023.

Getachew, A. (2009). The study of aerosol microphysical and optical parameters, total columnar ozone and water vapor content derived from sun photometer. Ph.D. thesis, Addis Ababa University.

Getachew, B., Manjunatha, B and Bhat, H.G. (2020). Spatio-temporal distribution of aerosol optical depth and cloud properties over Lake Tana Basin, Upper Blue Nile River Basin, Ethiopia. *Remote Sensing Applications: Society and Environment* **20:** 100–401.

Gitau, W., Ogallo, L., Camberlin, P and Okoola, R. (2013). Spatial coherence and potential predictability assessment of intraseasonal statistics of wet and dry spells over Equatorial Eastern Africa. *International Journal of Climatology* **33**: 2690–2705.

Grythe, H. (2017). Quantification of sources and removal mechanisms of atmospheric aerosol particles. Ph.D. thesis, Department of Environmental Science and Analytical Chemistry, Stockholm University.

Hansen, T.F., Pienaar, J and Orzack, S.H. (2008). A comparative method for studying adaptation to a randomly evolving environment. *Evolution* **62**: 1965–1977.

Homa, M.G., Tsidu, G.M and Nega, D.T.(2017). Stratospheric aerosol climatology over Ethiopia and retrieval of its size distribution. *Atmospheric Chemistry and Physics Discussions* **133**: 1–14.

Hopkins, K.D and Weeks, D.L. (1990). Tests for normality and measures of skewness and kurtosis: Their place in research reporting. *Educational and Psychological Measurement* **50**: 717–729.

Huang, J., Fu, Q., Su, J., Tang, Q., Minnis, P., Hu, Y., Yi, Y and Zhao, Q. (2009). Taklimakan dust aerosol radiative heating derived from CALIPSO observations using the Fu-Liou radiation model with CERES constraints. *Atmospheric Chemistry and Physics* **9**: 4011–4021.

Indeje, M., Semazzi, F.H and Ogallo, L.J. (2000). ENSO signals in East African rainfall seasons. *International Journal of Climatology* **20**: 19–46.

Ininda, J.M. (1994). Numerical simulation of the influence of the sea surface temperature anomalies on the east African seasonal: rainfall. PhD. thesis, University of Nairobi.

Ismael, H. (2015). The effectiveness of using MODIS products for monitoring climate change risks over the Nile Delta, Egypt. *International Journal of Environmental Monitoring and Analysis* **3**: 382–396.

Jin, J., Henzing, B and Segers, A. (2023). How aerosol size matters in aerosol optical depth (AOD) assimilation and the optimization using the Ångström exponent. *Atmospheric Chemistry and Physics* **23**: 1641–1660.

Justice, C.O., Vermote, E., Townshend, J.R., Defries, R., Roy, D.P., Hall, D.K., Salomonson, V.V., Privette, J.L., Riggs, G., Strahler, A., et al. (1998). The moderate resolution imaging spectroradiometer (MODIS): Land remote sensing for global change research. *IEEE Transactions on Geoscience and Remote Sensing* **36**(4): 1228–1249.

Kafle, D and Coulter, R. (2013). Micropulse lidar-derived aerosol optical depth climatology at ARM sites worldwide. *Journal of Geophysical Research: Atmospheres* **118**: 7293–7308.

Kalisa, W., Zhang, J., Igbawua, T., Henchiri, M., Mulinga, N., Nibagwire, D and Umuhoza, M. (2023). Spatial and temporal heterogeneity of air pollution in East Africa. *Science of the Total Environment* **886**: 163 734.

Kaufman, Y.J., Holben, B.N., Tanré, D., Slutsker, I., Smirnov, A and Eck, T.F. (2000). Will aerosol measurements from Terra and Aqua polar orbiting satellites represent the daily aerosol abundance and properties? *Geophysical Research Letters* **27**: 3861–3864.

Khan, R., Kumar, K.R., Zhao, T., Ullah, W and de Leeuw, G. (2021). Interdecadal changes in aerosol optical depth over Pakistan based on the MERRA-2 reanalysis data during 1980–2018. *Remote Sensing* **13**: 822.

Kharol, S.K., Badarinath, K., Sharma, A.R., Kaskaoutis, D and Kambezidis, H. (2011). Multiyear analysis of Terra/Aqua MODIS aerosol optical depth and ground observations over tropical urban region of Hyderabad, India. *Atmospheric Environment* **45**: 1532–1542.

Koukouli, M., Kazadzis, S., Amiridis, V., Ichoku, C., Balis, D and Bais, A. (2010). Signs of a negative trend in the MODIS aerosol optical depth over the Southern Balkans. *Atmospheric Environment* **44**: 1219–1228.

Kumar, K.R., Yin, Y., Sivakumar, V., Kang, N., Yu, X., Diao, Y., Adesina, A.J and Reddy, R. (2015). Aerosol climatology and discrimination of aerosol types retrieved from MODIS, MISR and OMI over Durban (29.88 S, 31.02 E), South Africa. *Atmospheric Environment* **117**: 9–18.

LeBlanc, S.E., Redemann, J., Flynn, C., Pistone, K., Kacenelenbogen, M., Segal-Rosenheimer, M., Shinozuka, Y., Dunagan, S., Dahlgren, R.P., Meyer, K., et al. (2020). Above-cloud aerosol optical depth from airborne observations<? xmltex\break?> in the southeast Atlantic. *Atmospheric Chemistry and Physics* **20**: 1565–1590.

Ledesma, R.D and Valero-Mora, P. (2019). Determining the number of factors to retain in EFA: An easy-to-use computer program for carrying out parallel analysis. *Practical Assessment, Research, and Evaluation* **12**: 2.

Levy, R.C., Mattoo, S., Sawyer, V., Shi, Y., Colarco, P.R., Lyapustin, A.I., Wang, Y and Remer, L.A. (2018). Exploring systematic offsets between aerosol products from the two MODIS sensors. *Atmospheric Measurement Techniques* **11**: 4073–4092.

Li, H., Zhang, M., Wang, L., Ma, Y., Qin, W and Gong, W. (2021). The effect of aerosol on downward diffuse radiation during winter haze in Wuhan, China. *Atmospheric Environment* **265**: 118 714.

Li, J., Carlson, B.E., Dubovik, O and Lacis, A.A. (2014). Recent trends in aerosol optical properties derived from AERONET measurements. *Atmospheric Chemistry and Physics* **14**: 12 271–12 289.

Li, Z., Rosenfeld, D and Fan, J. (2017). Aerosols and their impact on radiation, clouds, precipitation, and severe weather events. In: Oxford Research Encyclopedia of Environmental Science.

Liu, Y., Lin, T., Hong, J., Wang, Y., Shi, L., Huang, Y., Wu, X., Zhou, H., Zhang, J and de Leeuw, G. (2021). Multi-dimensional satellite observations of aerosol properties and aerosol types over three major urban clusters in eastern China. *Atmospheric Chemistry and Physics* **21**: 12 331–12 358

Loeb, N.G., Doelling, D.R., Wang, H., Su, W., Nguyen, C., Corbett, J.G., Liang, L., Mitrescu, C., Rose, F.G and Kato, S. (2018). Clouds and the earth’s radiant energy system (CERES) energy balanced and filled (EBAF) top-of-atmosphere (TOA) edition-4.0 data product. *Journal of Climate* **31**: 895–918.

Lu, H., Xie, M., Liu, B., Liu, X., Feng, J., Yang, F., Zhao, X., You, T., Wu, Z and Gao, Y. (2022). Impact of atmospheric thermodynamic structures and aerosol radiation feedback on winter regional persistent heavy particulate pollution in the Sichuan-Chongqing region, China. *Science of the Total Environment* **842**: 156 575.

Maggioni, V., Meyers, P.C and Robinson, M.D. (2016). A review of merged high-resolution satellite precipitation product accuracy during the Tropical Rainfall Measuring Mission (TRMM) Era. *Journal of Hydrometeorology* **17**: 1101–1117.

Makokha, J.W., Odhiambo, J.O and Godfrey, J.. (2017). Trend analysis of aerosol optical depth and angström exponent anomaly over East Africa. *Atmospheric and Climate Sciences* **7**: 588–603.

Mushtaq, Z., Sharma, M., Bangotra, P., Gautam, A.S and Gautam, S. (2022). Atmospheric aerosols: some highlights and highlighters, past to recent years. *Aerosol Science and Engineering* **6**: 135–145.

Myhre, G., Myhre, C., Samset, B and Storelvmo, T.(2013). Aerosols and their relation to global climate and climate sensitivity. *Nature Education Knowledge* **4**: 7.

Negash, T. (2019). Eritrea and Ethiopia: the federal experience. Routledge.

Ngaina, J.N. (2015). Modelling aerosol-cloud-precipitation interactions for weather modification in East Africa, Ph.D. thesis, University of Nairobi.

Ngaina, J.N., Mutai, B., Ininda, J and Muthama, J. (2014). Monitoring spatial-temporal variability of aerosol over Kenya. *Ethiopian Journal of Environmental Studies and Management* **7**: 244–252.

Okuda, T. (2013). Measurement of the specific surface area and particle size distribution of atmospheric aerosol reference materials. *Atmospheric Environment* **75**: 1–5.

Pagano, T.S and Durham, R.M. (1993). Moderate resolution imaging spectroradiometer (MODIS). *Sensor Systems for the Early Earth Observing System Platforms* **1939**: 2–17.

Parkinson, C.L. (2022). The Earth-observing aqua satellite mission: 20 years and counting. *Earth and Space Science* **9**: e2022EA002 481.

Patel, M.P and Application, S. (2016). Study of aerosol optical depth and black carbon concentration over dehradun and surroundings. Indian Institute of Remote Sensing (ISRO).

Roughgarden, J., Running, S.W and Matson, P.A. (1991). What does remote sensing do for ecology? *Ecology* **72**: 1918–1922.

Silleos, N. (2000). Introduction to remote sensing and geographical information systems. Thessaloniki, Giahoudi-Giapouli.

Simpson, J., Adler, R.F and North, G.R. (1988). A proposed tropical rainfall measuring mission (TRMM) satellite. *Bulletin of the American Meteorological Society* **69**: 278–295.

Smith, G., Priestley, K., Loeb, N., Wielicki, B., Charlock, T., Minnis, P., Doelling, D and Rutan, D. (2011). Clouds and Earth Radiant Energy System (CERES), a review: Past, present and future. *Advances in Space Research* **48**: 254–263.

Sporre, M. (2016). Aerosol-cloud-precipitation interactions-studied using combinations of remote sensing and in-situ data. Lund University. https://lup.lub.lu.se/search/publication/8521127. Online; accessed 19 July 2023.

Stephenson, D., Kumar, K.R., Doblas-Reyes, F., Royer, J., Chauvin, F and Pezzulli, S. (1999). Extreme daily rainfall events and their impact on ensemble forecasts of the Indian monsoon. *Monthly Weather Review* **127**: 1954–1966.

Symeonidis, P. (2017). Study of spatial and temporal variation of atmospheric optical parameters and their relation with PM 2.5 concentration over Europe using GIS technologies, Master Thesis in Geographical Information Science.

Thapa, M., Bhattarai, B., Gurung, S., Sapkota, B and Poudyal, K. (2016). Diurnal and monthly variation of aerosol optical depth and angstrom's parameters in Kathmandu Valley, Nepal. *Research Journal of Chemical Sciences* **6**: 40–44.

Theon, J.S. (1994). The tropical rainfall measuring mission (TRMM). *Advances in Space Research* **14**: 159–165.

Toledano, C., Cachorro, V., Berjon, A., De Frutos, A., Sorribas, M., De la Morena, B and Goloub, P. (2007). Aerosol optical depth and Ångström exponent climatology at El Arenosillo AERONET site (Huelva, Spain). *A Journal of the Atmospheric Sciences, Applied Meteorology and Physical Oceanography* **133**: 795–807.

Tongco, M.D.C. (2007).Purposive sampling as a tool for informant selection. *Ethnobotany Research & Applications* **5**: 147–158.

Torres-Delgado, E., Baumgardner, D and Mayol-Bracero, O.L. (2021). Measurement report: Impact of African aerosol particles on cloud evolution in a tropical montane cloud forest in the Caribbean. *Atmospheric Chemistry and Physics* **21**: 18 011–18 027.

Ustin, S.L and Middleton, E.M. (2021). Current and near-term advances in Earth observation for ecological applications. *Ecological Processes* **10**: 1–57.

Verma, S., Prakash, D., Soni, M and Ram, K. (2019). Atmospheric aerosols monitoring: Ground and satellite-based instruments. *Advances in Environmental Monitoring and Assessment.* IntechOpen London, UK. http://dx.doi.org/10.5772/intechopen.80489. Online; accessed 19 July 2023.

Washington, R and Todd, M.C. (2005). Atmospheric controls on mineral dust emission from the Bodélé Depression, Chad: The role of the low level jet. *Geophysical Research Letters* **32:** L17 701.

Wild, M and Liepert, B. (2010). The Earth radiation balance as driver of the global hydrological cycle. *Environmental Research* Letters 5 (2010) 025003.

Wu, J., Zhang, S., Yang, Q., Zhao, D., Fan, W., Zhao, J and Shen, C. (2021). Using particle swarm optimization to improve visibility-aerosol optical depth retrieval method. *Climate and Atmospheric Science* **4**: 49.

Yang, Z., Wang, J., Ichoku, C., Hyer, E and Zeng, J. (2013). Mesoscale modeling and satellite observation of transport and mixing of smoke and dust particles over northern sub-Saharan African region. *Journal of Geophysical Research* **118**: 12139-12157.

Yang, X., Zhao, C., Yang, Y and Fan, H. (2021). Long-term multi-source data analysis about the characteristics of aerosol optical properties and types over Australia. *Atmospheric Chemistry and Physics* **21**: 3803–3825.

Yu, X., Nichol, J., Lee, K.H., Li, J and Wong, M.S. (2022). Analysis of long-term aerosol optical properties combining AERONET sunphotometer and satellite-based observations in Hong Kong. *Remote Sensing* **14**: 5220.

Zhang, H., Yan, D., Zhang, B., Fu, Z., Li, B and Zhang, S. (2022). An operational atmospheric correction framework for multi-source medium high-resolution remote sensing data of China. *Remote Sensing* **14**: 5590.